
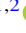





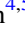
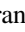







Consistent Dynamical and Stellar Masses with Potential Light IMF in Massive Quiescent Galaxies at $3 < z < 4$ Using Velocity Dispersions Measurements with MOSFIRE

James Esdaile^{1,2} , Karl Glazebrook^{1,2} , Ivo Labbé¹ , Edward Taylor¹ , Corentin Schreiber³ , Themiya Nanayakkara¹ , Glenn G. Kacprzak^{1,2} , Pascal A. Oesch^{4,5} , Kim-Vy H. Tran^{2,6,7} , Casey Papovich^{8,9} , Lee Spitler^{10,11} , and Caroline M. S. Straatman¹² 

¹ Centre for Astrophysics and Supercomputing, Swinburne University of Technology, Melbourne, VIC 3122, Australia; jesdaile@swin.edu.au

² ARC Centre for Excellence in All-Sky Astrophysics in 3D (ASTRO 3D), Australia

³ Department of Physics, University of Oxford, Clarendon Laboratory, Parks Road, Oxford OX1 3PU, UK

⁴ University of Geneva, Observatoire de Genève, Chemin des Maillettes 51, CH-1290 Versoix, Switzerland

⁵ Cosmic Dawn Center (DAWN), University of Copenhagen, Vibenshuset, Lyngbyvej 2, DK-2100 Copenhagen, Denmark

⁶ School of Physics, University of New South Wales, Kensington, Australia

⁷ Department of Astronomy, University of Washington, USA

⁸ Department of Physics and Astronomy, Texas A&M University, College Station, TX, 77843-4242 USA

⁹ George P. and Cynthia Woods Mitchell Institute for Fundamental Physics and Astronomy, Texas A&M University, College Station, TX, 77843-4242 USA

¹⁰ Department of Physics and Astronomy, Macquarie University, Sydney, NSW 2109, Australia

¹¹ Research Centre in Astronomy, Astrophysics & Astrophotonics, Macquarie University, Sydney, NSW 2109, Australia

¹² Department of Physics and Astronomy, Ghent University, Krijgslaan 281 S9, B-9000 Gent, Belgium

Received 2020 October 19; revised 2021 January 19; accepted 2021 January 28; published 2021 February 22

Abstract

We present the velocity dispersion measurements of four massive $\sim 10^{11} M_{\odot}$ quiescent galaxies at $3.2 < z < 3.7$ based on deep H and K -band spectra using the Keck/MOSFIRE near-infrared spectrograph. We find high velocity dispersions of order $\sigma_e \sim 250 \text{ km s}^{-1}$ based on strong Balmer absorption lines, and we combine these with size measurements based on HST/WFC3 F160W imaging to infer dynamical masses. The velocity dispersions are broadly consistent with the high stellar masses and small sizes. Together with evidence for quiescent stellar populations, the spectra confirm the existence of a population of massive galaxies that formed rapidly and quenched in the early universe $z > 4$. Investigating the evolution at constant velocity dispersion between $z \sim 3.5$ and $z \sim 2$, we find a large increase in effective radius 0.35 ± 0.12 dex and in dynamical-to-stellar mass ratio $\langle \log(M_{\text{dyn}}/M^*) \rangle$ of 0.33 ± 0.08 dex, with low expected contribution from dark matter. The dynamical masses for our $z \sim 3.5$ sample are consistent with the stellar masses for a Chabrier initial mass function (IMF), with the ratio $\langle \log(M_{\text{dyn}}/M_{\text{Ch}}^*) \rangle = -0.13 \pm 0.10$ dex suggesting an IMF lighter than Salpeter may be common for massive quiescent galaxies at $z > 3$. This is surprising in light of the Salpeter or heavier IMFs found for high velocity dispersion galaxies at $z \sim 2$ and cores of present-day ellipticals, which these galaxies are thought to evolve into. Future imaging and spectroscopic observations with resolved kinematics using the upcoming James Webb Space Telescope could rule out potential systematics from rotation and confirm these results.

Unified Astronomy Thesaurus concepts: [Galaxy evolution \(594\)](#); [Galaxy kinematics \(602\)](#); [High-redshift galaxies \(734\)](#)

1. Introduction

Recent spectroscopic detections of massive quiescent galaxies (MQG) at $z > 3$ (Marsan et al. 2017; Glazebrook et al. 2017; Schreiber et al. 2018a; Valentino et al. 2020; Forrest et al. 2020) present challenges for galaxy evolution theory due to their rapid early formation, high stellar masses, and abrupt quenching, within the first 1.5 billion years of the universe. In addition, these galaxies have substantial old stellar populations and studying them can provide insights into the formation conditions of stars during the epoch of reionization.

Tensions between theoretical predictions and observations of MQG at $3 < z < 4$ have existed since their discovery, with number densities in the Illustris (Wellons et al. 2015) and Mufasa (Davé et al. 2016) simulations a factor of ten lower than observed (Schreiber et al. 2018a). The latest generations of hydrodynamical simulations, such as Illustris TNG (Nelson et al. 2019), have started to close the gap in number densities (see discussion in Merlin et al. (2019)), although observed galaxies still seem to form their stars and quench earlier (Schreiber et al. 2018a). Critical in these comparisons is that the stellar masses of observed MQGs are correct, because

lower-mass galaxies are more common and AGN feedback invoked by simulations to quench galaxies depends on mass. Independent confirmation of the stellar masses is therefore needed.

Measuring stellar velocity dispersions of a galaxy provides a strong consistency check on its stellar mass and size. Massive $\sim 10^{11} M_{\odot}$ quiescent galaxies at $z \sim 2$ are found to have extremely compact rest-frame optical sizes with half-light sizes of order $r_e = 1\text{--}2 \text{ kpc}$ (van der Wel et al. 2014). The sizes are much smaller than those of their descendants at low redshift, implying strong size growth with time, most likely driven by minor merging (Naab et al. 2009; Hopkins et al. 2009). The combination of mass and size implies that the predicted stellar velocity dispersions are very high ($\sim 200\text{--}400 \text{ km s}^{-1}$), which can be tested with deep ground-based NIR spectroscopy. High velocity dispersions have since been confirmed at $1 < z < 2$ (e.g., van Dokkum et al. 2008; Bezanson et al. 2013; van de Sande et al. 2013; Belli et al. 2014a, 2017), but the situation at $z > 3$ is much less clear. Extremely compact $\sim 0.5 \text{ kpc}$ sizes have been reported from HST F160W (Straatman et al. 2015) and ground-based adaptive optics K -band imaging (Kubo et al. 2018),

2–3 times smaller than at $z \sim 2$. However, H -band F160W images from HST trace the rest-frame UV, which may be a poor proxy for the distribution of stellar mass, and corresponding velocity dispersion measurements are still lacking.

Finally, having kinematic and size information offers the opportunity to explore the relation between dynamical mass and stellar mass of quiescent galaxies at $z > 3$. Systematic changes of M_{dyn}/M^* with time could point to changes in the fraction of dark matter within the effective radius or variation in the initial stellar mass function IMF (e.g., see Mendel et al. (2020), and discussion therein). The dense cores of the most massive early type galaxies today have large fractions of low-mass stars (Salpeter IMF or heavier) (e.g., Cappellari et al. 2013a; van Dokkum et al. 2017), therefore one might expect similarly dense galaxies at high redshift to have bottom-heavy IMFs as well.

Massive quiescent galaxies $z > 3$ are a factor 3–10 times less numerous and an order of magnitude fainter in rest-frame optical (from redshift dimming) compared to $z \sim 2$. Obtaining the high-resolution and high signal-to-noise spectra required for measuring stellar velocity dispersions of these galaxies is very challenging due to the requirement of deep near-infrared spectra to target stellar populations in the rest-frame optical.

Presently, there have been no measurements of the stellar velocity dispersions of MQG at $z > 3$ with accompanying HST imaging in literature to date. Recently, Tanaka et al. (2019) presented a stellar velocity dispersion measurement of a quenching galaxy at $z = 4.01$ with a high stellar velocity dispersion consistent with the stellar mass. However, there was no HST imaging available, and this limited the confidence on size constraints when considering the dynamical mass.

This paper presents the measurement of four velocity dispersions of massive quiescent galaxies $3.2 < z < 3.7$ using deep H and K -band spectra (taken from the Schreiber et al. (2018a) sample), all with WFC3/F160W HST imaging enabling high-resolution size measurements. This is the largest sample of the highest-redshift massive quiescent galaxies with integrated stellar velocity dispersion measurements to date.

The paper is organized as follows: Section 2 outlines the galaxy sample, data reduction and galaxy properties, Section 3 outlines the analysis of the spectra including velocity dispersion measurements and dynamical mass modeling, and Section 4 presents a discussion of the results and conclusions. Throughout this paper, we use AB magnitudes and adopt a flat Λ CDM cosmology with $\Omega_{\Lambda} = 0.7$, $\Omega_M = 0.3$ and $H_0 = 70 \text{ km s}^{-1} \text{ Mpc}^{-1}$.

2. Sample and Data

2.1. Spectral Sample

The data sample comprises deep H - and K -band spectra of photometrically selected MQGs at $3 < z < 4$. The parent sample was preselected from multiwavelength photometric catalogs: the ZFOURGE and 3D-HST catalogs (Skelton et al. 2014; Straatman et al. 2016) across the CANDELS fields EGS/AEGIS, GOODS-South, COSMOS, and UDS (Grogin et al. 2011; Koekemoer et al. 2011). The galaxies were selected to have photometric redshifts of $3 < z < 4$, massive $\log(M^*/M_{\odot}) \geq 10.3$, and UVJ color-color selected to separate quiescent from star-forming galaxies (Whitaker et al. 2011). Spectroscopic follow-up of 12 galaxies resulted in 8 galaxies

that are spectroscopically confirmed at $z > 3$ with clear detection of the continuum (Schreiber et al. 2018a). For the four brightest galaxies ($K < 22.5$), we were able to measure robust velocity dispersions. It is possible that this sample is biased toward recently quenched galaxies that are brighter and show stronger Balmer absorption lines. Spectral completeness is a complex function of depth, wavelength coverage, redshift, magnitude, size, and SED shape. Despite the potential bias toward lower M/L ratios and younger post-starburst populations, the properties are consistent with the broader UVJ-selected quiescent galaxy sample in Schreiber et al. (2018a) in terms of the mass, size, and UVJ color distributions, and hence there is no indication that such a bias might influence our results or conclusions.

2.2. Observations and MOSFIRE Reduction

All spectral data are taken from the Schreiber et al. (2018a) sample with no new observations. A detailed description for the observations and data reduction is presented in Schreiber et al. (2018a), for which a summary follows. All galaxies were observed in the H - and K -band spectra using the MOSFIRE (McLean et al. 2012) spectrograph, a multi-object infrared spectrograph installed on the Keck I telescope, on top of Maunakea in Hawaii. The galaxies were observed on several masks across multiple nights, all observed with standard ABBA exposures, nodding along the slit with a $0''.7$ slit for mask configurations. Seeing conditions were $0''.63$ – $0''.8$ in H -band and $0''.55$ – $0''.75$ in K -band. Individual exposures lasted 120 and 180 s in the H - and K -bands, respectively. The total exposure times for the four galaxies in our sample are as follows: ZF-COS-20115 had 4.2h and 14.4h in H - and K -band, respectively, and 3D-EGS-18996, 3D-EGS-40032, and 3D-EGS-31322 all had 0.8h and 4.8h in H - and K -band, respectively.

The data were reduced using the publicly available 2015A MOSFIRE DRP release. Uncertainties are determined for each spectral element by bootstrapping the individual exposures, which produces errors that are larger than the formal uncertainties from the MOSFIRE DRP. The 1D spectra are binned (inverse-variance weighted) by a factor of three, which reduces spectrally-correlated noise while increasing the signal-to-noise ratio per bin. The final binning of each 1D spectrum is 6 \AA pixel^{-1} , close to the nominal $R \sim 3000$ resolution of MOSFIRE with $0''.7$ slits. The median signal-to-noise ratios of the spectra are in the range $\text{SNR}_K = 5$ – 7 . The reduced spectra are shown in Figure 1.

2.3. Spectral Energy Distribution Modeling

Stellar masses and star formation rates were calculated in Schreiber et al. (2018a) using FAST++, which is a C++ implementation of FAST (Kriek et al. 2009) developed by Corentin Schreiber.¹³ These quantities are used in this paper without any additional analysis; however, a brief description of the methods and inputs are described here for reference. FAST++ performs simultaneous fitting of the UV-IRAC photometry and NIR spectra, and is able to handle a large parameter grid for modeling, complex star formation histories (SFHs), and additional observational constraints such as L_{IR} priors. Stellar mass, SFR, dust extinction, and stellar age are all derived by

¹³ <https://github.com/cschreib/fastpp>

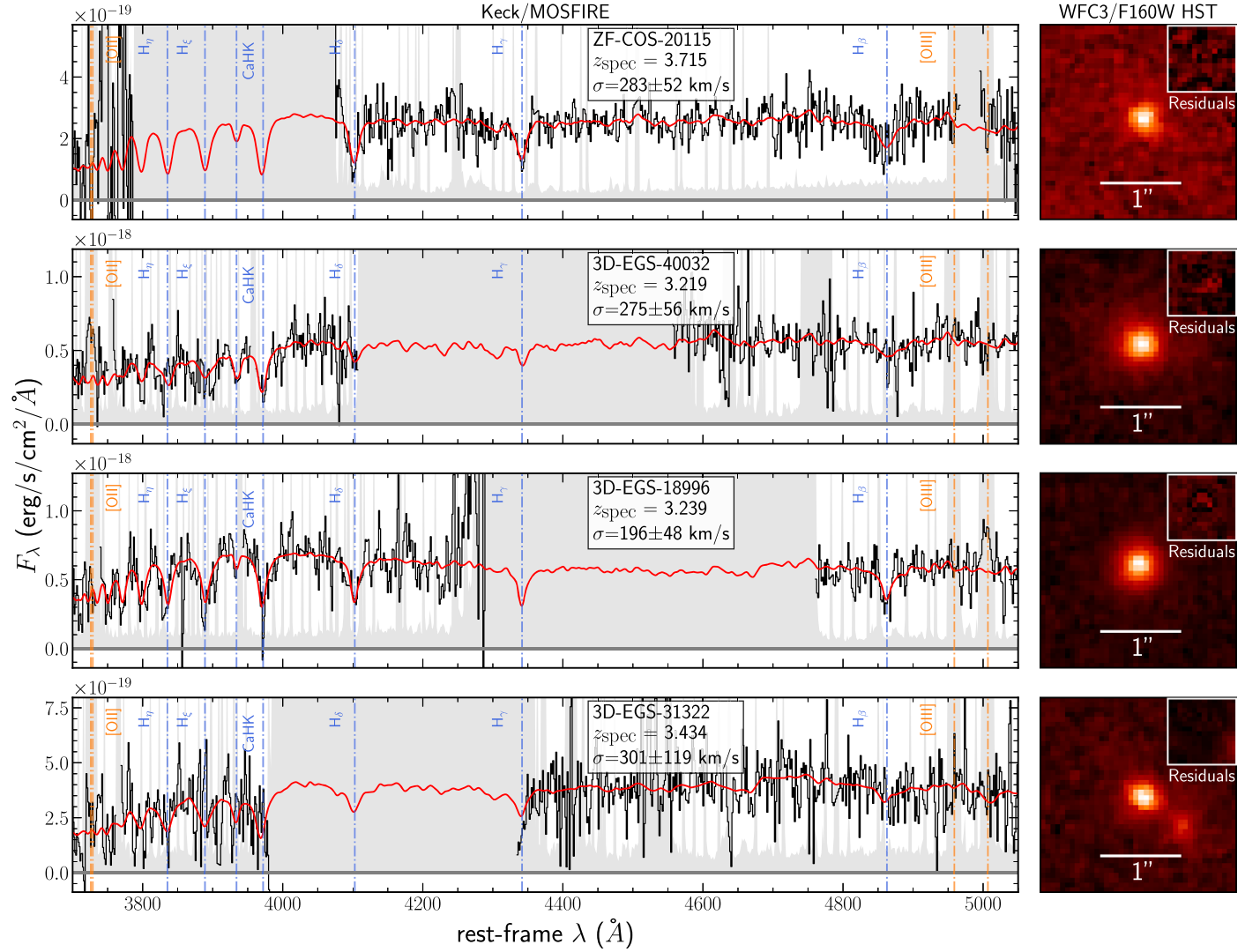


Figure 1. Left panel: velocity dispersion measurements for four massive quiescent galaxies at $3.2 < z < 3.7$. Black solid line is the 1D galaxy spectrum, solid red line is the pPXF best-fit spectrum, and gray bars denote the 1σ uncertainty. Gray vertical bands indicate where there is either no flux determined or masked regions due to low sky transmission or emission line regions, and these have been masked in the pPXF fitting. Spectra are shown as observed flux, corrected for slit-loss as in Schreiber et al. (2018a). Vertical blue and orange dashed-dotted lines show absorption and emission line features from left to right: [O II], H_γ, H_δ, Ca II H & K, H_β, H_γ, H_β, and [O III]. Right panel: *H*-band WFC3/F160W HST image stamps used in determining half-light radius r_e and other physical properties as in Table 2. Top right inset shows the residuals from our size modeling with the same pixel scale and stretch as the HST images.

Table 1
Galaxy Properties from Literature

ID	z	H (AB mag.)	K (AB mag.)	M^* ($10^{11}M_\odot$)	A_v (AB mag.)	SFR ₁₀ ^a ($M_\odot \text{ yr}^{-1}$)	sSFR (Gyr^{-1})	t_{quench} ^b (Gyr)	z_{form} ^c
ZF-COS-20115	3.715	24.39 ± 0.03	22.43 ± 0.02	$1.15^{+0.16}_{-0.09}$	$0.3^{+0.1}_{-0.1}$	$0.0^{+0.7}_{-0.0}$	$0.00^{+0.01}_{-0.00}$	$0.51^{+0.19}_{-0.24}$	$6.1^{+0.8}_{-0.7}$
3D-EGS-40032	3.219	22.92 ± 0.02	21.59 ± 0.03	$2.03^{+0.16}_{-0.14}$	$0.4^{+0.1}_{-0.1}$	$6.1^{+3.7}_{-3.4}$	$0.03^{+0.02}_{-0.02}$	$0.51^{+0.14}_{-0.20}$	$5.0^{+1.3}_{-0.4}$
3D-EGS-18996	3.239	22.75 ± 0.01	21.60 ± 0.02	$0.98^{+0.04}_{-0.06}$	$0.0^{+0.1}_{-0.0}$	$1.0^{+1.0}_{-0.9}$	$0.01^{+0.01}_{-0.01}$	$0.33^{+0.09}_{-0.10}$	$4.3^{+0.3}_{-0.1}$
3D-EGS-31322	3.434	23.72 ± 0.03	22.20 ± 0.04	$0.98^{+0.12}_{-0.08}$	$0.3^{+0.2}_{-0.2}$	$0.0^{+2.3}_{-0.0}$	$0.00^{+0.02}_{-0.00}$	$0.28^{+0.25}_{-0.02}$	$4.9^{+1.6}_{-0.4}$

Notes.

^a SFR averaged over the last 10 Myr.

^b Time since the SFR has fallen below 10% of the peak SFR period.

^c Redshift where 50% of the stellar mass has formed.

fitting Bruzual & Charlot (2003) models assuming Chabrier (2003) IMF and a Calzetti (2001) dust attenuation law. SFH modeling was carried out using a parametric form with exponential rise, decline, and quenching. The final SFH modeling involved marginalizing over these parametric

quantities to produce values such as the current SFR and stellar mass, as well as additional nonparametric quantities describing the SFH, such as quenching and formation epochs. The stellar mass for ZF-COS-20115, originally determined in Glazebrook et al. (2017), was revised after deblending of a

Table 2
Structural and Kinematic Properties

ID	σ_e (km s ⁻¹)	r_e (kpc)	n	q_{obs}	M_{dyn} (10 ¹¹ M _⊙)	log(M_{dyn}/M^*)
ZF-COS-20115	283 ± 52	0.66 ± 0.08	4.10 ± 0.99	0.61 ± 0.07	0.72 ± 0.27	-0.2 ^{+0.16} _{-0.25}
3D-EGS-40032	275 ± 56	2.40 ± 0.19	3.72 ± 0.18	0.77 ± 0.02	2.59 ± 0.78	0.11 ^{+0.13} _{-0.20}
3D-EGS-18996	196 ± 48	0.63 ± 0.05	3.34 ± 0.21	0.83 ± 0.02	0.36 ± 0.13	-0.44 ^{+0.15} _{-0.23}
3D-EGS-31322	301 ± 119	0.61 ± 0.05	4.76 ± 0.85	0.53 ± 0.03	0.71 ± 0.42	-0.14 ^{+0.21} _{-0.43}

nearby ALMA-detected galaxy, reducing the stellar mass by 0.17 dex. A detailed description of the modeling is presented in Schreiber et al. (2018a). Table 1 shows a summary of the stellar masses, SFR, and other derived quantities from Schreiber et al. (2018a). As the random uncertainties on the stellar mass are very low, we adopt a minimum 0.08 dex error reflecting systematic errors associated with using different spectral energy distribution (SED) models (Ilbert et al. 2010; Pforr et al. 2012). To check for systematic errors when comparing to lower-redshift samples from the literature, we compared the stellar masses of the $1.4 < z < 2.1$ sample of Mendel et al. (2020) based on FSPS to those derived with FAST at a median offset of -0.05 dex.

The modeling indicates that the stellar masses are high ($1-2 \times 10^{11} M_{\odot}$), dust attenuation is low, and the galaxies formed in a brief burst about 0.5–1.0 Gyr earlier, with very low levels of ongoing star formation (specific star formation rates $\text{sSFR} < 0.03 \text{ Gyr}^{-1}$) based on SED fitting. This picture is confirmed by analyzing the spectra, which show deep Balmer series and Ca II H&K absorption lines for all galaxies. For one galaxy, 3D-EGS-18996, we find [O III] in emission, and for another, 3D-EGS-40032, [O II] emission is weakly detected. Nevertheless, all galaxies have $\text{sSFR} \lesssim 0.1 \text{ Gyr}^{-1}$ based on [O II] emission or H β absorption alone; a factor of ~ 15 below the galaxy main sequence at this redshift (see Schreiber et al. 2018a). In addition, ZF-COS-20115 has stringent limits on dust obscured SFR ($\text{sSFR} < 0.1 \text{ Gyr}^{-1}$) based on a nondetection in deep ALMA imaging (Schreiber et al. 2018b).

2.4. Structural Properties

The structural properties were measured on H -band WFC3/F160W HST images, in a manner similar to that of van der Wel et al. (2012), albeit without the use of their pipeline software GALAPAGOS. Single-component Sérsic profiles were fit using GALFIT (Peng et al. 2010), providing the half-light radius along the semimajor axis r_e^{sma} , Sérsic index n , and axis ratio $q = b/a$. We use semimajor axis rather than harmonic mean radius ($r_e^{\text{sma}} \sqrt{ab}$), as it has been shown to be less sensitive to galaxy shape (Cappellari et al. 2013a). We manually subtracted the local background for each source by measuring the mode of the pixel distribution after masking sources. Faint neighboring sources at $r > 1.3''$ were masked, while close neighbors were fitted simultaneously. Point-spread functions (PSFs) were taken from van der Wel et al. (2012). The results are shown in Table 2.

We find excellent agreement with the results of van der Wel et al. (2014), all within uncertainties except for 3D-EGS-40032, which has a nearby neighbor and is smaller by 25%. All sources are compact ($r_e = 0.08-0.3''$) with very high integrated SNR $\sim 50-150$ (within $r_e < 0.3''$), resulting in small formal uncertainties. Comparing results using different PSFs for similar sources, Straatman et al. (2015) found 7% variation in

r_e , which we add in quadrature to account for systematic error due to PSF choice. While F160W samples rest-frame near-UV (3500 Å) and sizes of lower-redshift samples are usually measured in the rest-frame optical, Straatman et al. (2015) find no significant wavelength dependence for massive compact quiescent galaxies at $z \sim 2.5$. We therefore do not apply a correction for band-shifting. Applying the correction of van der Wel et al. (2014) to rest-frame r -band would reduce the effective radius by 18%.

We compared our total fluxes used in SED fitting to the total flux based on the Sérsic fit, finding good agreement within 2%–3%. Therefore, we did not adjust our stellar mass for missing light.

3. Analysis

3.1. Velocity Dispersion

We measure the observed stellar line-of-sight velocity dispersions (LOSVD) of our galaxy sample using pPXF (Cappellari 2017), which utilizes a maximum penalized likelihood approach to fitting spectra to a library of stellar or stellar population templates and determines galaxy kinematics. For our analysis, we use the Indo-US stellar library templates (Valdes et al. 2004) with $R \sim 4200$, which are smoothed to the binned resolution of the reduced spectra of $R \sim 3000$.

We mask out portions of the spectra where telluric atmospheric absorption bands are significant and also where the spectra are potentially impacted by [O II] or [O III] emission lines. Good fits to the continuum are obtained for all galaxies, as shown in Figure 1. We do not introduce additional freedom (e.g., additive/multiplicative polynomial) to attempt better match to the continuum. The results are not sensitive to this choice. As our 1D spectra are optimally extracted with a Gaussian kernel based on the PSF, i.e., seeing-limited, we correct our velocity dispersions within the aperture to velocity dispersions within r_e as per van de Sande et al. (2013), resulting in a mean correction of 0.02 dex. The measured velocity dispersions including aperture corrections are shown in Table 2. We find large velocity dispersions for all galaxies ranging from 200 – 300 km s⁻¹.

We derive LOSVD uncertainties using Monte Carlo simulations. We take the best-fit spectrum to the observed data from pPXF and perturb its flux 1000 times by a random value drawn from a Gaussian with a standard deviation consistent with the uncertainties of the observed spectrum (determined as outlined in Section 2.2). The LOSVD for each iteration is determined and the standard deviation of all 1000 Monte Carlo simulations is used as the error for the LOSVD. These errors are larger than the formal pPXF uncertainties by a factor of 1.1–2.2.

To test potential systematic errors of our measurements, we ran pPXF for multiple scenarios. We exclude the H β line and

find consistent results, suggesting that emission line-infilling is not significant for these galaxies. To explore dependence on stellar library, we use the MILES stellar library (Sanchez-Blazquez et al. 2006; Falcón-Barroso et al. 2011) and find that the results agree within the uncertainties.

To investigate stability and consistency, we take the best-fit spectrum for each galaxy and smooth it to simulate different velocity dispersions, perturbing the flux by observational errors as per the Monte Carlo simulation above. We are able to recover velocity dispersions for the range 150–500 km s⁻¹ within the pPXF uncertainties, which shows that we should be able to recover dispersions and uncertainties from data of this quality. The median residuals for the recovered velocity dispersions are small ($\lesssim 17$ km s⁻¹), compared to the typical errors from our MCMC analysis, and therefore do not indicate significant systematic error.

Finally, we note that, for 3D-EGS-31322, the spectroscopic redshift probability within $\Delta z \pm 0.01$ is $p = 84\%$ from Schreiber et al. (2018a), due to a small secondary peak in the redshift probability distribution at $z = 3.51$, and is therefore considered less certain compared to the rest of the sample ($p = 100\%$). We fail to recover a velocity dispersion at the secondary redshift. Therefore, we are more confident in the quoted redshift, due to the robustness of the recovered velocity dispersion, which is a higher-order effect (line width compared to line center). Additionally, we note that its inclusion in the analysis that follows in Section 4 does not change the qualitative result presented in the discussion therein.

3.2. Dynamical Masses

The tight relationship between size, mass, and stellar velocity dispersion for elliptical galaxies is understood to come from virial equilibrium conditions. For dynamically pressure-supported galaxies, an estimate of the total mass can be derived from the following equation:

$$M_{\text{dyn}} = \frac{\beta(n)\sigma_e^2 r_e}{G}, \quad (1)$$

where r_e is the half-light radius, σ_e is the LOSVD within the half-light radius, $\beta(n)$ is the virial coefficient, which is used to account for structural and orbital nonhomology, and G is the gravitational constant. We use an analytical approximation for the virial coefficient as a function of Sérsic index, n , described by Cappellari et al. (2006):

$$\beta(n) = 8.87 - 0.831n + 0.0241n^2, \quad (2)$$

where β has been calibrated to estimate the total mass for nearby elliptical galaxies in the SAURON and ATLAS^{3D} samples (Cappellari et al. 2006, 2013a). For errors in dynamical masses, we add in quadrature the errors for the LOSVD, r_e , and Sérsic indices. The errors are mostly dominated by the error in the LOSVD, with 60%–90% contribution compared to the error of r_e and n . We neglect covariance between r_e and n and M_{dyn} and M^* (due to luminosity-derived stellar masses) because they are subdominant. The dynamical masses, alongside the LOSVD and structural properties, are shown in Table 2. The derived dynamical masses are substantial, ranging from 0.4–2.6 $\times 10^{11} M_{\odot}$.

4. Discussion and Conclusions

Figure 2 presents the structural and kinematic properties of our sample compared to MQG samples from lower redshifts. At low redshift $z \sim 0.1$, we show UVJ selected galaxies in the SDSS/GAMA sample. For this sample, the velocity dispersions are taken from the SDSS Legacy Sample from SDSS DR14 (Abolfathi et al. 2018) with Sérsic-fit parameters from (Kelvin et al. 2012) and stellar mass estimates (Taylor et al. 2011) from GAMA DR3 (Baldry et al. 2018). At intermediate redshift, we adopt the sample of 58 MQG from $1.4 < z < 2.1$ from Mendel et al. (2020), which includes other recent literature (Cappellari et al. 2009; Newman et al. 2010; Toft et al. 2012; Bezanson et al. 2013; van de Sande et al. 2013; Belli et al. 2014a, 2014b; Barro et al. 2016; Belli et al. 2017) using observations from VLT/KMOS, VLT/XShooter, and Keck/MOSFIRE. At $z > 3$, we include the quenching galaxy (sSFR ~ 0.2 Gyr⁻¹) at $z = 4.01$ recently reported by Tanaka et al. (2019).¹⁴ All the M_{dyn} values for the various redshift populations have been calculated in a manner consistent with that described in Section 3.2.

The first significant result for our $3 < z < 4$ MQG sample is that the dynamical masses are broadly consistent with the derived SED masses for a Chabrier (2003) IMF (see Figure 2). The stellar mass is an important input in AGN feedback models in hydrodynamical simulations (Merlin et al. 2019), and therefore its confirmation is further evidence of the existence of a population of quiescent galaxies within the first two billion years, with early star formation and rapid quenching.

Further insights on this population come from inspecting the r_e , σ_e , and M^* planes of Figure 2. The size–stellar mass distributions suggests that massive quiescent galaxies at $3 < z < 4$ are significantly more compact than at $z \sim 2$ (Straatman et al. 2015; Tanaka et al. 2019). However, the marginally resolved HST/WFC3 sizes are based on rest-frame near-UV light, which may not reflect the distribution of stellar mass (although SED modeling shows no evidence of significant dust attenuation in the integrated properties). The high stellar velocity dispersions measured here provide independent evidence for the concentration of large stellar mass within small radii. Overall, the distributions of r_e , σ_e , and M_{dyn} at fixed stellar mass suggests the MQG population continues to change with increasing redshift toward smaller sizes, larger velocity dispersions, and lower dynamical mass.

Tracing populations across redshift is complicated by progenitor bias, whereby newly quenched galaxies enter the population that are not progenitors of the lower-redshift populations. One way to relate descendants and progenitors is to select galaxies at fixed cumulative number density (e.g., Van Dokkum et al. 2010). Alternatively, galaxies can be selected at fixed central velocity dispersion (e.g., Mendel et al. 2020). Central velocity dispersions have been shown in simulations to be relatively stable through dissipationless mergers, which are the main size-growth mechanism for MQGs in simulations (Naab et al. 2009; Hopkins et al. 2009) and supported by observations (van de Sande et al. 2013; Belli et al. 2014a, 2017; Mendel et al. 2020). Matching galaxies from the $z \sim 2$ sample within $\Delta\sigma < 0.05$ dex of the galaxies in our sample, we find an average size growth since $3 < z < 4$ of

¹⁴ We note that HST imaging was not available for this galaxy, so an assumed $\beta = 5$ was used for the M_{dyn} value, with the conservative errors in r_e derived in Tanaka et al. (2019). We excluded this galaxy from M_{dyn}/M^* comparisons.

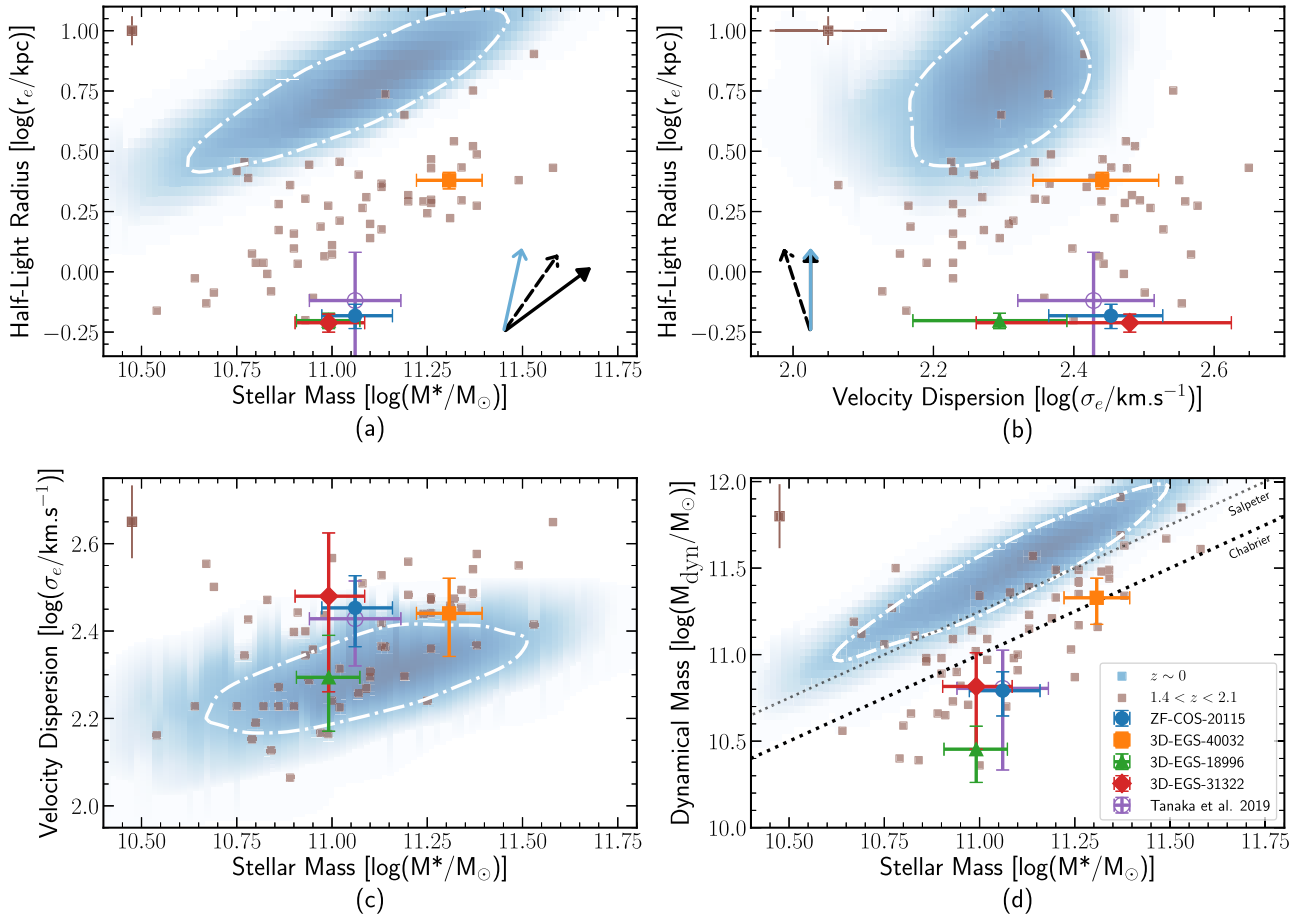


Figure 2. Comparison of physical properties for massive quiescent galaxies at various epochs. In each panel, the same galaxies are shown: ZF-COS-20115, 3D-EGS-40032, 3D-EGS-18996, and 3D-EGS-31322 are shown as the blue circle, orange square, green triangle, and red diamond respectively. Quenching galaxy from Tanaka et al. (2019) is shown as an open purple circle. Brown squares represent the $1.4 < z < 2.1$ sample from Mendel et al. (2020). The SDSS/GAMA $z \sim 0.1$ sample is shown as a log density shading in blue, with white dashed-dotted contour representing the 68th percentile. Median errors for $z \sim 2$ population are shown for reference in the upper left portion of each panel. Panel (a): $r_e - M^*$. Panel (b): $r_e - \sigma_e$. Dashed line and solid line black arrows show the expected minor and major merger evolution for the quantities in each panel, with blue arrows showing the observed evolution at fixed σ_e . Panel (c): $M^* - \sigma_e$. Panel (d): dynamical mass versus stellar mass from SED modeling. Dotted black line shows the 1v1 line for a Chabrier IMF; dotted gray line shows that for a Salpeter IMF. Dynamical mass for the Mendel et al. (2020) sample in panel (d) corresponds to M_{VIR} from their paper.

0.35 ± 0.12 dex, stellar mass increase of 0.05 ± 0.05 dex, and increase of $\Delta \log(M_{\text{dyn}}/M^*) = 0.33 \pm 0.08$ dex. Taken at face value, the size growth is stronger than is easily accounted for with minor mergers (although at low significance). This has also been observed at lower redshift in similar studies (Newman et al. 2012; Mendel et al. 2020), and may mean other processes such as stellar mass loss from AGN feedback (Fan et al. 2008; Choi et al. 2018) could be contributing to the evolution in size.

Figure 3 shows the offset in the ratio of dynamical to stellar mass, sometimes called the IMF offset parameter α , which is found to correlate with central velocity dispersion σ_e and appears to not have evolved significantly since $z \sim 2$ (Cappellari et al. 2013b; Mendel et al. 2020). Together with IMF gradients found in nearby massive ellipticals (van Dokkum et al. 2017), the observations support a formation scenario in which compact massive galaxies at high redshift form the central regions of massive ellipticals today, with the outer parts built up later through (mostly minor) mergers. This scenario predicts that high velocity dispersion galaxies at $z > 2$ have Salpeter-like or heavier IMFs, as is the case at $z \sim 2$. It is therefore surprising to find such low dynamical-to-stellar mass ratios at $3 < z < 4$.

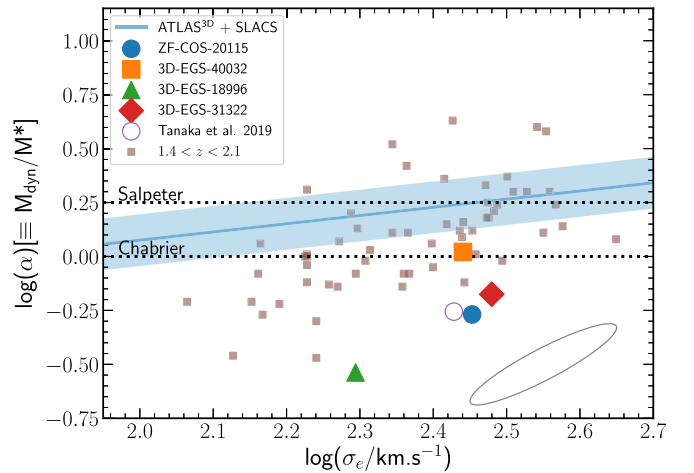


Figure 3. IMF parameter: α vs. σ_e . Sample and marker layout are the same as in Figure 2, but instead using the mass-follows-light models for the $z \sim 2$ sample from Mendel et al. (2020), which have a tighter $\alpha - \sigma$ relation. Error ellipse in the bottom right represents the correlated errors for the $3.2 < z < 3.7$ sample. Dotted lines are for a Chabrier and Salpeter IMF normalization. Blue solid line is the IMF- σ_e relation for the ATLAS^{3D}+SLACS sample derived in Posacki et al. (2015), with blue shaded area representing the 1σ scatter.

It is possible that our assumptions about the galaxy kinematics are incorrect: more complex kinematic structures such as rotationally supported galaxies, as seen in strongly lensed $z \sim 2$ MQGs (Toft et al. 2017; Newman et al. 2018), could increase M_{dyn} by a factor 2 if $V_r/\sigma \sim 2$, allowing for IMFs steeper than Chabrier. In addition, the distribution of F160W light (rest-frame 3500 Å) may not follow the distribution of stellar mass if the galaxies have M/L gradients. We note that the dark matter fraction in the central parts of massive quiescent galaxies at $z \sim 2$ is estimated to be small $f_{\text{DM}}[< r_e] = 7\%$ (Mendel et al. 2020), and it is expected to be even smaller at $z > 3$ given the extremely small effective radii $r_e < 1$ kpc.

The most extreme galaxies with very low M_{dyn}/M^* ratios, such as 3D-EGS-18996, could even point toward a top-heavy IMF, which may be present in galaxies with intense starbursts (Weidner et al. 2013) from which MQGs are likely formed. To evaluate the impact of a top-heavy IMF, we refitted our sample for stellar mass using a range of high-mass slopes in the IMF. Starting from a Chabrier IMF with a slope of $\gamma = dn/d\log M = -1.35$, we flattened the slope to $\gamma = -1$ and only found a reduction in stellar mass by 0.1 dex. The reason for the modest reduction is that, in older stellar populations, high-mass stars have mostly disappeared, so flattening of the IMF slope has little effect.

Without resolved kinematics and better stellar population modeling of these galaxies, it is currently not possible to distinguish between the various scenarios. In addition, observational biases and selection biases cannot be ruled out. To better understand the $3 < z < 4$ MQG population, it is imperative to not only increase the sample size to see if the observed trends remain, but also utilize the upcoming James Webb Space Telescope to provide resolved rest-frame optical imaging and deep integrated spectra to constrain the IMF, alongside resolved spectra to enable rotational velocity measurements to determine dynamical mass.

Some of the data presented herein were obtained at the W. M. Keck Observatory, which is operated as a scientific partnership among the California Institute of Technology, the University of California, and the National Aeronautics and Space Administration. The Observatory was made possible by the generous financial support of the W. M. Keck Foundation.

The authors wish to recognize and acknowledge the very significant cultural role and reverence that the summit of Maunakea has always had within the indigenous Hawaiian community. We are most fortunate to have the opportunity to conduct observations from this mountain.

The authors would like to acknowledge the referee for useful feedback, as well as Trevor Mendel and Richard McDermid for helpful discussions during the preparation of the paper.

J. E., K. G., G. K., and K. V. T. acknowledge support by the Australian Research Council Centre of Excellence for All Sky Astrophysics in 3-Dimensions (ASTRO 3D), through project number CE170100013.

K. G. and T.N. also acknowledge support from Laureate Fellowship FL180100060. G. G. K. also acknowledges the support of the Australian Research Council through Discovery Project grant DP170103470.






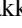






C. P. acknowledge generous support from the George P. and Cynthia Woods Mitchell Institute for Fundamental Physics and Astronomy at Texas A&M University. This material is based

upon work supported by the National Science Foundation under Cooperative Agreement No. AST0525280

C. M. S. S. acknowledges support from the Research Foundation – Flanders (FWO) through Fellowship 12ZC120N.

Software: pPXF (Cappellari et al. 2006; Cappellari 2017), GALFIT (Peng et al. 2010), astropy (Robitaille et al. 2013; Price-Whelan et al. 2018), SExtractor (Bertin & Arnouts 1996).

ORCID iDs

James Esdaile  <https://orcid.org/0000-0001-6941-7662>
 Karl Glazebrook  <https://orcid.org/0000-0002-3254-9044>
 Ivo Labbé  <https://orcid.org/0000-0002-2057-5376>
 Edward Taylor  <https://orcid.org/0000-0002-3958-0343>
 Corentin Schreiber  <https://orcid.org/0000-0003-0942-5198>
 Themiya Nanayakkara  <https://orcid.org/0000-0003-2804-0648>
 Glenn G. Kacprzak  <https://orcid.org/0000-0003-1362-9302>
 Pascal A. Oesch  <https://orcid.org/0000-0001-5851-6649>
 Kim-Vy H. Tran  <https://orcid.org/0000-0001-9208-2143>
 Casey Papovich  <https://orcid.org/0000-0001-7503-8482>
 Lee Spitler  <https://orcid.org/0000-0001-5185-9876>
 Caroline M. S. Straatman  <https://orcid.org/0000-0001-5937-4590>

References

- Abolfathi, B., Aguado, D. S., Aguilar, G., et al. 2018, *ApJS*, 235, 42
 Baldry, I. K., Liske, J., Brown, M. J., et al. 2018, *MNRAS*, 474, 3875
 Barro, G., Faber, S. M., Dekel, A., et al. 2016, *ApJ*, 820, 120
 Belli, S., Genzel, R., Förster Schreiber, N. M., et al. 2017, *ApJL*, 841, L6
 Belli, S., Newman, A. B., & Ellis, R. S. 2014a, *ApJ*, 783, 117
 Belli, S., Newman, A. B., Ellis, R. S., & Konidaris, N. P. 2014b, *ApJL*, 788, L29
 Bertin, E., & Arnouts, S. 1996, *A&AS*, 117, 393
 Bezanson, R., Van Dokkum, P., Van De Sande, J., Franx, M., & Kriek, M. 2013, *ApJL*, 764, L8
 Bruzual, G., & Charlot, S. 2003, *MNRAS*, 344, 1000
 Calzetti, D. 2001, *PASP*, 113, 1449
 Cappellari, M. 2017, *MNRAS*, 466, 798
 Cappellari, M., Bacon, R., Bureau, M., et al. 2006, *MNRAS*, 366, 1126
 Cappellari, M., Di Serego Alighieri, S., Cimatti, A., et al. 2009, *ApJ*, 704, 34
 Cappellari, M., McDermid, R. M., Alatalo, K., et al. 2013b, *MNRAS*, 432, 1862
 Cappellari, M., Scott, N., Alatalo, K., et al. 2013a, *MNRAS*, 432, 1709
 Chabrier, G. 2003, *PASP*, 115, 763
 Choi, E., Somerville, R. S., Ostriker, J. P., Naab, T., & Hirschmann, M. 2018, *ApJ*, 866, 91
 Davé, R., Thompson, R., & Hopkins, P. F. 2016, *MNRAS*, 462, 3265
 Falcón-Barroso, J., Sánchez-Blázquez, P., Vazdekis, A., et al. 2011, *A&A*, 532, A95
 Fan, L., Lapi, A., De Zotti, G., & Danese, L. 2008, *ApJL*, 689, L101
 Forrest, B., Annunziatella, M., Wilson, G., et al. 2020, *ApJL*, 890, L1
 Glazebrook, K., Schreiber, C., Labbé, I., et al. 2017, *Natur*, 544, 71
 Grogin, N. A., Kocevski, D. D., Faber, S. M., et al. 2011, *ApJS*, 197, 2011
 Hopkins, P. F., Hernquist, L., Cox, T. J., Keres, D., & Wuyts, S. 2009, *ApJ*, 691, 1424
 Ilbert, O., Salvato, M., Le Floc’H, E., et al. 2010, *ApJ*, 709, 644
 Kelvin, L. S., Driver, S. P., Robotham, A. S., et al. 2012, *MNRAS*, 421, 1007
 Koekemoer, A. M., Faber, S. M., Ferguson, H. C., et al. 2011, *ApJS*, 197, 36
 Kriek, M., Van Dokkum, P. G., Labbé, I., et al. 2009, *ApJ*, 700, 221
 Kubo, M., Tanaka, M., Yabe, K., et al. 2018, *ApJ*, 867, 1
 Marsan, Z. C., Marchesini, D., Brammer, G. B., et al. 2017, *ApJ*, 842, 21
 McLean, I. S., Steidel, C. C., Epps, H. W., et al. 2012, *Proc. SPIE*, 8446, 84460J
 Mendel, J. T., Beifiori, A., Saglia, R. P., et al. 2020, *ApJ*, 899, 87
 Merlin, E., Fortuni, F., Torelli, M., et al. 2019, *MNRAS*, 490, 3309
 Naab, T., Johansson, P. H., & Ostriker, J. P. 2009, *ApJ*, 699, 178
 Nelson, D., Springel, V., Pillepich, A., et al. 2019, *ComAC*, 6, 2
 Newman, A. B., Belli, S., Ellis, R. S., & Patel, S. G. 2018, *ApJ*, 862, 126
 Newman, A. B., Ellis, R. S., Bundy, K., & Treu, T. 2012, *ApJ*, 746, 162

- Newman, A. B., Ellis, R. S., Treu, T., & Bundy, K. 2010, [ApJL](#), **717**, L103
- Peng, C. Y., Ho, L. C., Impey, C. D., & Rix, H. W. 2010, [AJ](#), **139**, 2097
- Pforr, J., Maraston, C., & Tonini, C. 2012, [MNRAS](#), **422**, 3285
- Posacki, S., Cappellari, M., Treu, T., Pellegrini, S., & Ciotti, L. 2015, [MNRAS](#), **446**, 493
- Price-Whelan, A. M., Sipőcz, B. M., Günther, H. M., et al. 2018, [AJ](#), **156**, 123
- Robitaille, T. P., Tollerud, E. J., Greenfield, P., et al. 2013, [A&A](#), **558**, A33
- Sanchez-Blazquez, P., Peletier, R. F., Jimenez-Vicente, J., et al. 2006, [MNRAS](#), **371**, 703
- Schreiber, C., Glazebrook, K., Nanayakkara, T., et al. 2018a, [A&A](#), **618**, A85
- Schreiber, C., Labbé, I., Glazebrook, K., et al. 2018b, [A&A](#), **611**, A22
- Skelton, R. E., Whitaker, K. E., Momcheva, I. G., et al. 2014, [ApJS](#), **214**, 24
- Straatman, C. M. S., Labbé, I., Spitler, L. R., et al. 2015, [ApJL](#), **808**, L29
- Straatman, C. M. S., Spitler, L. R., Quadri, R. F., et al. 2016, [ApJ](#), **830**, 51
- Tanaka, M., Valentino, F., Toft, S., et al. 2019, [ApJL](#), **885**, L34
- Taylor, E. N., Hopkins, A. M., Baldry, I. K., et al. 2011, [MNRAS](#), **418**, 1587
- Toft, S., Gallazzi, A., Zirm, A., et al. 2012, [ApJ](#), **754**, 3
- Toft, S., Zabl, J., Richard, J., et al. 2017, [Natur](#), **546**, 510
- Valdes, F., Gupta, R., Rose, J. A., Singh, H. P., & Bell, D. J. 2004, [ApJS](#), **152**, 251
- Valentino, F., Tanaka, M., Davidzon, I., et al. 2020, [ApJ](#), **889**, 93
- van de Sande, J., Kriek, M., Franx, M., et al. 2013, [ApJ](#), **771**, 85
- van der Wel, A., Bell, E. F., Haussler, B., et al. 2012, [ApJ](#), **788**, 28
- van der Wel, A., Franx, M., van Dokkum, P. G., et al. 2014, [ApJ](#), **788**, 28
- van Dokkum, P., Conroy, C., Villaume, A., Brodie, J., & Romanowsky, A. J. 2017, [ApJ](#), **841**, 68
- van Dokkum, P., Franx, M., Kriek, M., et al. 2008, [ApJ](#), **677**, L5
- Van Dokkum, P. G., Whitaker, K. E., Brammer, G., et al. 2010, [ApJ](#), **709**, 1018
- Weidner, C., Ferreras, I., Vazdekis, A., & Barbera, F. L. 2013, [MNRAS](#), **435**, 2274
- Wellons, S., Torrey, P., Ma, C.-P., et al. 2015, [MNRAS](#), **449**, 361
- Whitaker, K. E., Labbé, I., van Dokkum, P. G., et al. 2011, [ApJ](#), **735**, 86